PROCEEDINGS OF SCIENCE

Chiral Dynamics and the Pion Polarisability: Measurements at COMPASS

Jan Friedrich[*†] **on behalf of the COMPASS collaboration**
TU München
E-mail: jan.friedrich@cern.ch

The COMPASS experiment at CERN accesses pion-photon reactions via the Primakoff effect, where high-energetic pions react with the quasi-real photon field surrounding the target nuclei. Flagship channel is the Primakoff reaction in which a single real photon is produced, giving access to pion Compton scattering. From the measured cross-section shape, the pion polarisability is extracted and compared to earlier measurements as well as theoretical expectations.
At the same time, reactions with neutral or charged pions produced are measured and analyzed. At low energy in the pion-photon CMS, these reactions are governed by chiral dynamics and contain information relevant in the framework of chiral perturbation theory. At higher energies, resonances are produced and their radiative coupling is investigated.

International Winter Meeting on Nuclear Physics,
21-25 January 2013
Bormio, Italy

[*]Speaker.

[†]currently CERN, Geneva. Work supported by the German ministry BMBF, the Maier-Leibnitz-Labor der LMU und TU München, and the DFG Cluster of Excellence "Origin and Structure of the Universe".

PoS(Bormio 2013)030

1. Pion-photon reactions as test of chiral perturbation theory

Properties of the pions (π^-, π^0, π^+) are of crucial interest in understanding quantum chromodynamics (QCD), since the pion is the lightest system featuring confinement of quarks and gluons by the strong force. As such, the pions are identified in the framework of the low-momentum expansion of QCD, chiral perturbation theory (ChPT), as the Goldstone bosons emerging from the spontaneous breaking of chiral symmetry.

Pion-pion scattering has been studied in several approaches, *e.g.* in kaon decays, and successfully described within ChPT. In contrast, for pion-photon interactions even the most fundamental process of pion-photon, *i.e.* Compton, scattering has remained a riddle for the past 30 years: The leading structure-dependent term in this process is the polarisability, and its extraction from the first experimental data in 1983, confirmed by later experiments, resulted in values significantly higher than expected from most of the theoretical approaches. Clarifying this subject is the prime motivation for the experimental work presented here. On top of this, other pion-photon interactions with more pions in the final state came into reach, and are studied as well. This is, on the one hand, an independent research subject by itself, on the other hand, it represents a powerful check of the common aspects in the employed experimental techniques.

2. Embedding the process: Primakoff technique

Henry Primakoff proposed in 1951 [1] to make use of the intense electric field in the proximity of nuclei, which can be treated in a high-relativistic reference frame as a source of quasi-real photons, to study strongly-interacting particles. The original idea concerned the measurement of the π^0 lifetime by photon-photon fusion, but it was later realized that interactions of high-energetic hadrons with the nuclear Coulomb field represent similarly a scattering off the quasi-real photon density, and consequently the whole class of such hadron interactions is referred to as Primakoff reactions. The process is depicted in Fig. 1. The main contribution comes from impact parameters of the pions of a few nuclear radii, where the electric field is as strong as several 100 kV/fm. This displays how even a small polarisability as it is expected for hadrons can be measured, as a modification of the cross-section for bremsstrahlung emission. The cross-section formula for a Primakoff reaction $\pi^- A \to X^- A$ on a nucleus A reads, in one-photon exchange approximation (see *e.g.* [2]),

$$\frac{d\sigma}{ds\, dQ^2\, d\Phi} = \frac{\alpha}{\pi(s-m_\pi^2)} \cdot F_{\text{eff}}^2(Q^2) \cdot \frac{Q^2 - Q^2_{\text{min}}}{Q^4} \cdot \frac{d\sigma_{\pi\gamma}}{d\Phi} \tag{2.1}$$

and bases on the factorization into the quasi-real photon density multiplying the cross-section $d\sigma_{\pi\gamma}/d\Phi$ for the real-photon subprocess $\pi^-\gamma \to X^-$. Mandelstam-s is the squared total energy in the $\pi^-\gamma$ subsystem, Q^2 is the momentum transfer to the nucleus A, $\alpha \simeq 1/137$ is the fine structure constant, m_π the rest mass of the charged pion, $Q_{\text{min}} = (s - m_\pi^2)/2p$ is the minimum momentum transfer for given s and beam momentum p. $F_{\text{eff}}^2(Q^2)$ is the form factor of the target nucleus with charge Z. It is $F_{\text{eff}}^2(Q^2) \approx Z^2$ when $Q^2 \ll 10^{-3}\,\text{GeV}^2/c^2$ and in addition s is sufficiently small, such that the longitudinal compontent Q_L given in size approximately by Q_{min} is negligible. For the first process of interest, the final-state X^- is again $\pi^-\gamma$ such that the involved subprocess is pion

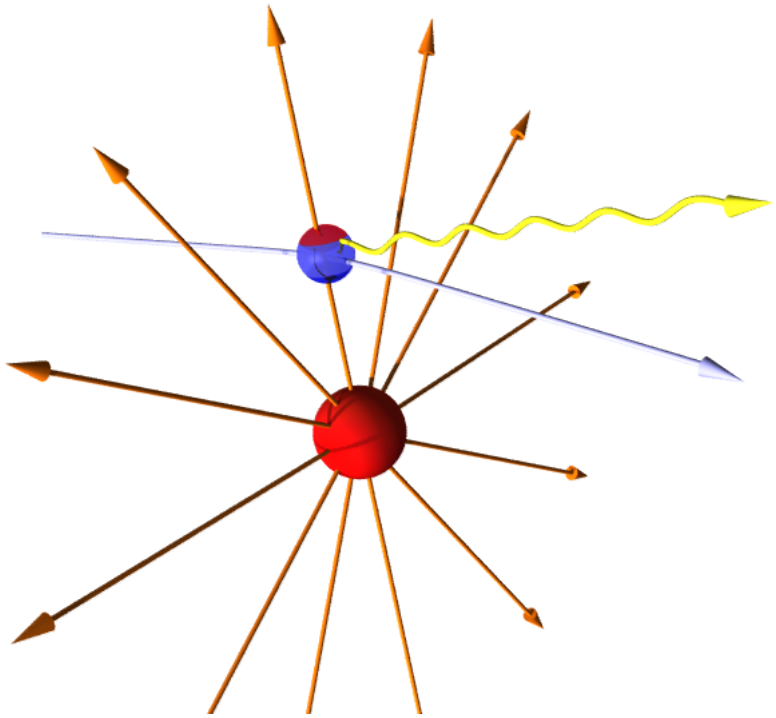

Figure 1: Visualization of the Primakoff Compton process: A high-energetic pion scatters in the electric field of a nucleus. For the magnetic contribution, it is to be realized that the nucleus passing the pion at high velocity represents an electric current inducing a magnetic field at the position of the pion.

Compton scattering $\pi^-\gamma \to \pi^-\gamma$. The respective cross-section reads

$$\frac{d\sigma_{\pi\gamma}}{d\Omega_{cm}} = \frac{\alpha^2(s^2z_+^2 + m_\pi^4 z_-^2)}{s(sz_+ + m_\pi^2 z_-)^2} - \frac{\alpha\, m_\pi^3\,(s-m_\pi^2)^2}{4s^2(sz_+ + m_\pi^2 z_-)} \cdot \\ \cdot \left(z_-^2(\alpha_\pi - \beta_\pi) + \frac{s^2}{m_\pi^4} z_+^2(\alpha_\pi + \beta_\pi) - \frac{(s-m_\pi^2)^2}{24s} z_-^3(\alpha_2 - \beta_2) \right) \tag{2.2}$$

where $z_\pm = 1 \pm \cos\theta_{cm}$ and θ_{cm} is the scattering angle in the $\pi^-\gamma$ center-of-momentum system, and the pion structure enters through the electric and magnetic polarisabilities α_π and β_π. In the following, the sum $\alpha_\pi + \beta_\pi$ which is expected to be small, and also the influence of the quadrupole polarisabilities α_2 and β_2 is neglected. Then, the relative effect of the polarisability $\alpha_\pi = -\beta_\pi$ on the cross-section, Eq. 2.1, integrated in the small-momentum transfer region $Q^2 \leq 10^{-3}\,\mathrm{GeV}^2/c^2$ and depending only on the fraction of energy transfered from the incoming pion beam to the emitted photon, $x_\gamma = E_\gamma/E_{beam}$, can be simplified into

$$R = \frac{\sigma(x_\gamma)}{\sigma_{\alpha_\pi=0}(x_\gamma)} = 1 - \frac{3}{2}\cdot\frac{m_\pi^3}{\alpha}\cdot\frac{x_\gamma^2}{1-x_\gamma}\,\alpha_\pi. \tag{2.3}$$

This relation is used to extract the polarisability from the measurement of the photon energy spectrum in the the Primakoff process $\pi^- Z \to \pi^-\gamma\, Z$ on a nucleus with charge Z, as it has been done

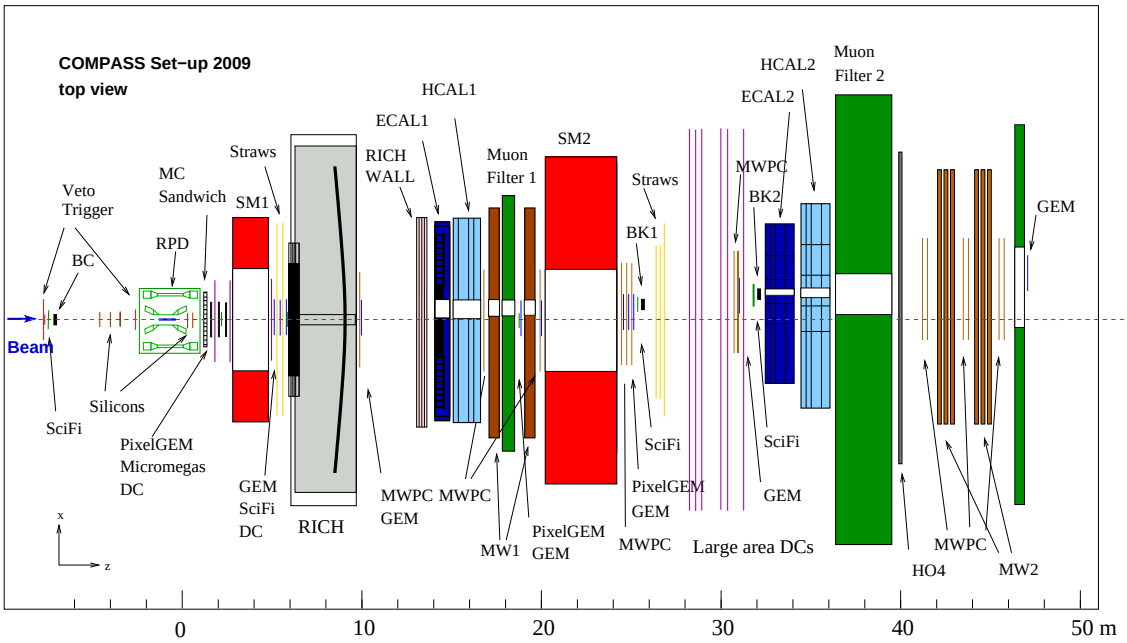

Figure 2: Layout of the COMPASS setup for hadron beam as used in the beam times of 2008 and 2009. A detailed description of the employed detectors is found e.g. in Reference [17]. The spectrometer magnets SM1 and SM2, surrounded by tracking detectors and followed by the calorimeters, constitute the two stages of the setup.

in the first measurement of this kind at Serpukhov [3].

3. Pion polarisability measurement at COMPASS

The COMPASS experiment deploys secondary hadron and tertiary muon beams from the CERN 450 GeV super proton synchrotron (SPS). Its multi-purpose detector concept allows for a wide range of investigations in hadron physics, with high-precision and high-rate capable tracking, particle identification and calorimetry in both stages of the magnetic spectrometer. The layout of the setup is shown in Fig. 2. The two stages are optimized for low and high momentum particles, respectively, and allow a momentum determination of better than 1% in a wide range, from about 1 GeV up to the beam momentum in the range of 200 GeV.

The measurement of the pion polarisability has been one of the original goals of the proposal for the COMPASS experiment. After a pilot run in the year 2004, the data presented in the following have been collected in a two-week beam time in 2009, with significant improvements in the calorimetry and the trigger system which based on the detailed analysis of the 2004 data. One of the conclusions along with preparing the data taking in 2009 [4] was that lead is not a favorable target material despite the high nuclear charge Z, since the radiative corrections due to multiple photon exchange and screening are large and represent a non-negligible source of systematic uncertainty. Consequently, the measurement was performed with a 4 mm thick nickel disk as nuclear target.

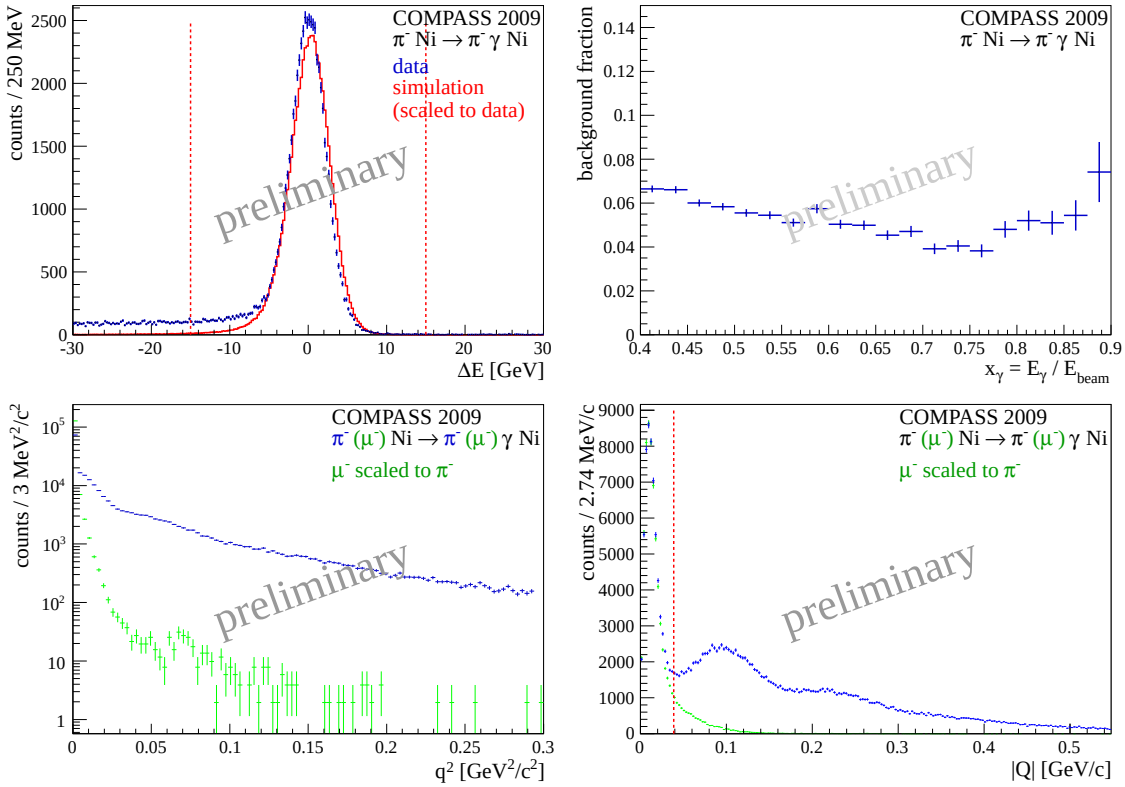

Figure 3: Energy balance of the reaction π^- Ni $\to \pi^-\gamma$ Ni (top left), background fraction (top right), and momentum transfer spectra in q^2 and $|Q|$ (bottom left and right, respectively) compared to those of the μ^- Ni $\to \mu^-\gamma$ Ni control measurements. The cuts applied to the data are indicated as vertical dashed lines.

The 190 GeV negative-charge secondary hadron beam from the SPS contains more than 97% pions, which are distinguished from kaons by Cherenkov detectors. A unique feature of the pion polarisability measurement at COMPASS is that the beam can be switched, within less than an hour, from hadron to muon beam, and the spectrometer is specialized to muon identification due to the broad physics program with muon beams. For the polarisability measurement, this allows for control measurements with muon beam, for which the theoretical expectation of the relevant bremsstrahlung process μ^- Ni$\to \mu^-\gamma$ Ni is completely determined by quantum electrodynamics (QED).

Reactions of the type π^- Ni $\to \pi^-\gamma$ Ni are selected by requiring the measurement of one negatively-charged scattered particle trajectory, that forms with the incoming pion trajectory a vertex consistent with an interaction in the nickel target, and a high-energetic shower in the electromagnetic calorimeter (ECAL), by which energy and momentum direction of the emitted photon can be reconstructed. Exclusive reactions are selected by energy conservation in the process π^- Ni $\to \pi^-\gamma$ Ni as depicted in Fig. 3, the upper-left graph showing the peak attributed to exclusive events in $\Delta E = E_{beam} - E_{\pi'} - E_\gamma \approx 0$, neglecting the (tiny) nuclear recoil energy. The width of the peak $\sigma \approx 2.6$ GeV is well in agreement with the simulation, reflecting mainly the resolution of the ECAL. The pion data show a non-exclusive background contribution, visible as a tail at negative

values of ΔE. Those stem from diffractive processes, mainly those with neutral pions in the final state, leading to a very similar ECAL response as the intended single-photon events. Their contribution is not included in the simulation, instead it is estimated from events with identified π^0. The result is a fraction of about 5%, slightly depending on the photon energy (top-right graph in Fig. 3), and is subtracted in the further analysis steps. The muon data do not feature such diffractive contributions. Their exclusivity peak is in full agreement with the simulation, and has a similar width as that of the pion data.

Photon exchange is identified by the strong increase of interaction probability at extremely small momentum transfer, as given by the quasi-real photon density term of Eq. 2.1. This "Primakoff peak" enters in the usual q^2 distribution, shown in the bottom-left graph of Fig. 3, only in the very first bin. Its details are better displayed in the variable $|Q| = |\vec{q}|$ shown in the bottom-right graph. The peak position as given by Eq. 2.1 would be around $1\,\mathrm{MeV}/c$, however in the data it is smeared with the experimental resolution of about $10\,\mathrm{MeV}/c$. On the scale of the incoming beam momentum of $190\,\mathrm{GeV}/c$, this is an excellent value steming from an angular resolution for the photon and the scattered pion with respect to the incoming pion direction of about $30\,\mu$rad. This is reached by determining the position of the electromagnetic showers of the photons in the ECAL, about 32 m downstream of the target, with a spatial resolution of 1.2 mm, and the track of the scattered pion with a spatial resolution of about $10\,\mu$m in the microstrip silicon detectors employed about 0.5 m downstream of the target. These features of the $|Q|$ distribution are also well described by the simulation, which fully matches in the muon case and lacks the salient additional pattern due to diffractive processes in the pion case. Photon exchange is selected by the cut indicated in the $|Q|$ distribution.

For the determination of the polarisability, the photon energy spectrum is examined according to Eq. 2.3. In the case of muon beam, the shape of the distribution is in excellent agreement with the simulation as shown in the upper graphs of Fig. 4. The size of the "false polarisability" signal, in agreement with zero within the fit uncertainty, of $\pm 0.6 \cdot 10^{-4}$ fm^3 is taken as an estimate for apparative imperfections not described by the simulation, *e.g.* concerning the tracking.

In the case of pion beam, the experimental spectrum has been corrected for the background estimation shown in Fig. 3, and is divided by the simulation, in which the bremsstrahlung cross-section for a pointlike spin-0 boson has been taken. The result of this procedure is shown in the lower graphs of Fig. 4. By fitting the distribution according to Eq. 2.3, the pion polarisability is determined from the COMPASS 2009 data to be $\alpha_\pi = (1.9 \pm 0.7_{stat}) \cdot 10^{-4}$ fm^3.

Radiative corrections have been applied on the level of the simulation event-wise, starting from the published calculations [5, 6] for the case of pion and muon Compton scattering, respectively, and extrapolating to the Primakoff kinematics at $Q^2 \neq 0$. The small difference between the corrections for pion and muon stem from their spin-0 and spin-$\frac{1}{2}$ nature, respectively. The error involved in the approximation $Q^2 \approx 0$ has been shown to be below 10% of the correction itself [4] and thus negligible. Along with the uncertainty of the vacuum polarisation and multiple-photon exchange corrections, the uncertainty of the radiative corrections to the determination of the pion polarisability has been estimated to be about $\pm 0.3 \cdot 10^{-4}$ fm^3, and this value is included in the list of systematic uncertainties in Tab. 1.

An additional background contained in the data stems from scattering of the beam particles off the electrons in the target. Since the recoiling electrons may lose practically all their energy by

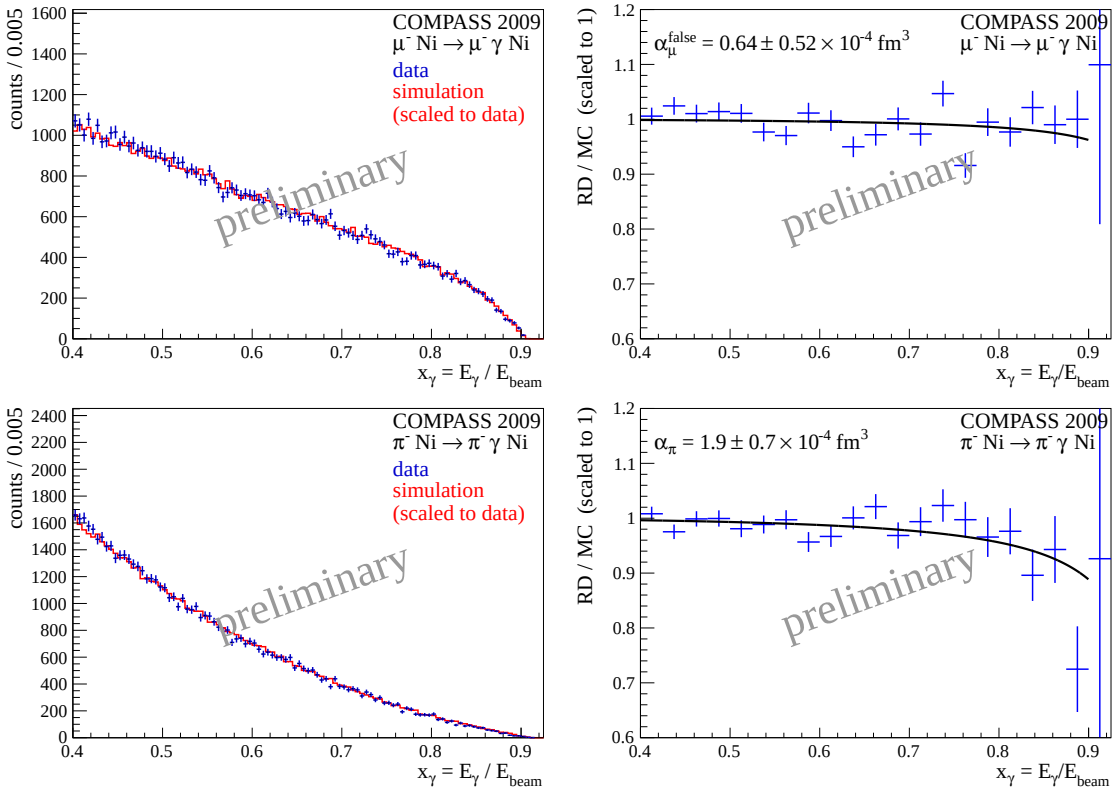

Figure 4: Control measurement with muons μ^- Ni $\to \mu^- \gamma$ Ni (top) and determination of the pion polarisability through the process π^- Ni $\to \pi^- \gamma$ Ni (bottom).

source of systematic uncertainty	estimated magnitude
tracking	0.6
radiative corrections	0.3
background subtraction in Q	0.4
pion-electron scattering	0.2
quadratic sum	0.8

Table 1: Systematic uncertainty estimates for the pion polarisability measurement (on 68% confidence level).

bremsstrahlung, this leads to a signature very similar to the intended process of photon emission when scattering off the nulcei. The contribution of this process has been investigated, and its impact on the polarisability determination included as systematic uncertainty in Tab. 1.

Summing all discussed systematic uncertainty contributions as summarized in Tab. 1, leads to a total of $\pm 0.8 \cdot 10^{-4}$ fm^3. So, the preliminary COMPASS result for the pion polarisability from the 2009 data is

$$\alpha_\pi = (1.9 \pm 0.7_{stat} \pm 0.8_{sys}) \cdot 10^{-4} \text{ fm}^3. \tag{3.1}$$

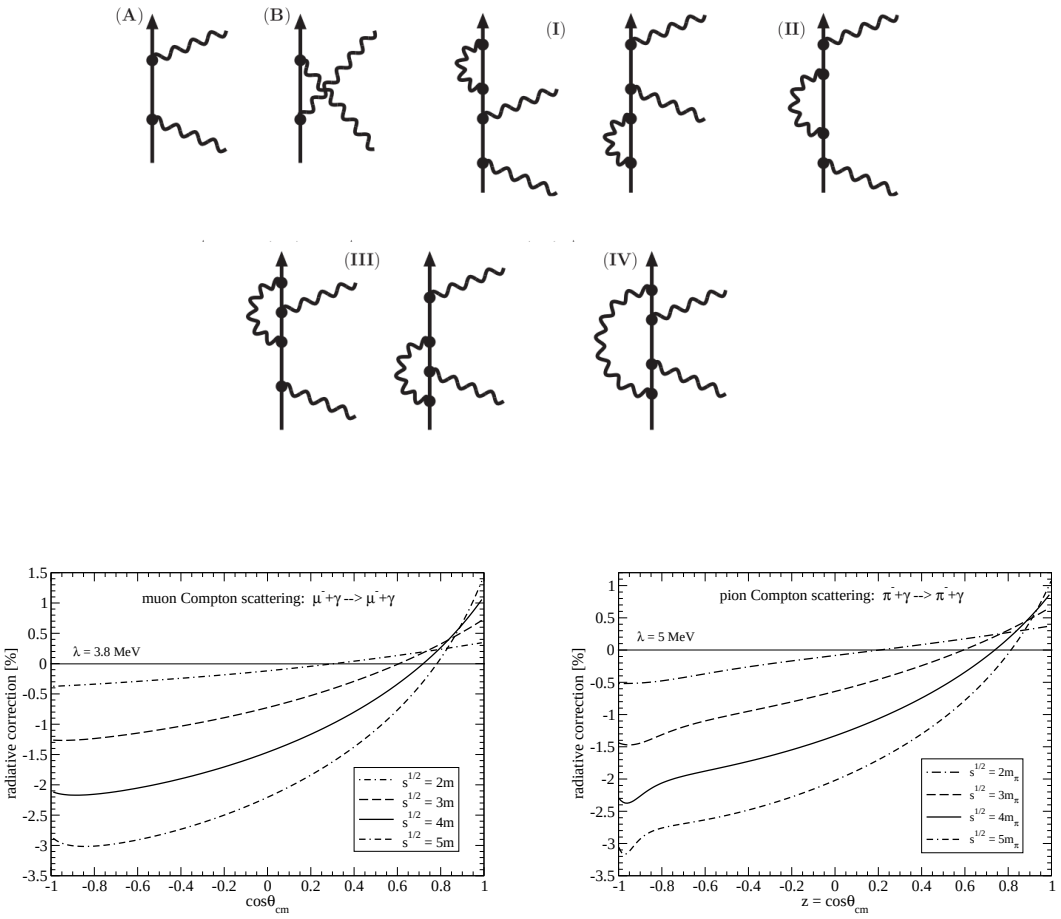

Figure 5: Electromagnetic radiative corrections for muon and pion Compton scattering. Examplarily, the Feynman graphs for the virtual corrections in the muon are shown (top part of the figure). For the pion, there are more graphs due to the additional point-couplings in case of a spin-0 particle [5]. The lower graphs (from [5, 6]) show the radiative corrections, to be employed as multiplicative factor to the non-radiative process, for different CM-energies in the region of interest for the pion polarisability measurement.

4. Discussion of the pion polarisability result

The presented preliminary COMPASS value for the pion polarisability is compared to previous experimental results in Fig. 6. Historically (left graph) the first result obtained at Serpukhov [3] had been confirmed much later by the dedicated experiment on radiative pion photoproduction at MAMI [7]. In the mean time, the available data on $\gamma\gamma \to \pi^+\pi^-$ at e^-e^+-colliders were re-interpreted by several authors [8, 9, 10, 11] claiming very different values for the pion polarisability, inspired by the assumptions on pion dynamics and the related low-energy constants that enter in this interpretation. Later on, it has been proven that there is no conflict between ChPT and dispersion theory [12, 13].

In that regard, the COMPASS result is in significant tension with the earlier experimental determinations of the pion polarisability, as the ideogram representation in Fig. 6 (right) shows, where only the dedicated experiments for the pion polarisability are included. Instead, the new

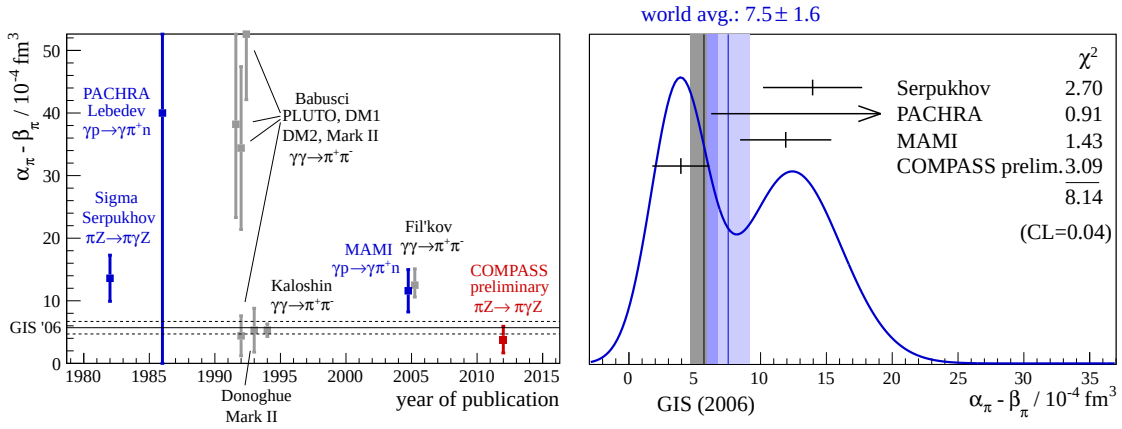

Figure 6: Placement of the preliminary COMPASS result on the pion polarisability in the world data (left) and the ideogram in "PDG style" [15] (right). Plots are from [16], where also a full discussion of the experimental data is found. The symbol GIS06 refers to the theoretical prediction as given in Reference [14].

result is found in good agreement with the expectation of chiral perturbation theory [14].

In view of the small value obtained for the pion polarisability in this analysis, it is of high interest what the data taken in the year 2012 at COMPASS with a very similar setup as described here will show. For this data set, the statistical uncertainty is expected to be a factor of three smaller and the polarisability signature of Fig. 4 accordingly clearer. This data set will also allow the extraction of α_π and β_π independently, as well as the determination of the quadrupole polarisability $\alpha_2 - \beta_2$. In addition, the first value for the kaon polarisability is in reach, using the identified kaon component of the beam and employing the same analysis technique as for the pion.

5. Chiral dynamics in Primakoff pion production processes

Along with refining the analysis described above, further processes on chiral dynamics in reach with the same COMPASS data were investigated [2]. Since long, the chiral anomaly in the process $\pi^-\gamma \to \pi^-\pi^0$ is of interest, however the analysis of this channel is still underway.

The detailed study of two-pion production at low energy is also not yet finished for the neutral-pion case $\pi^-\gamma \to \pi^-\pi^0\pi^0$. For the charged case $\pi^-\gamma \to \pi^-\pi^-\pi^+$, however, the analysis [17] of the data from the pilot run in the year 2004 has been completed, and is discussed in the following subsection.

5.1 $\pi^-\gamma \to \pi^-\pi^-\pi^+$ process at low final-state mass

The three charged-pion final state mass spectrum obtained in Primakoff kinematics off lead nuclei is shown in Fig. 7. While the region above about 1 GeV exhibits the usual shape including three-pion resonances discussed in the next subsection, the low-mass tail is of specific interest in terms of chiral dynamics: Since the tails of known resonances play only a minor role, and the relative pion momenta are low, the kinematics lies in the region where ChPT is applicable. ChPT provides predictions for the absolute cross section to leading [4] and next-to-leading [19] order.

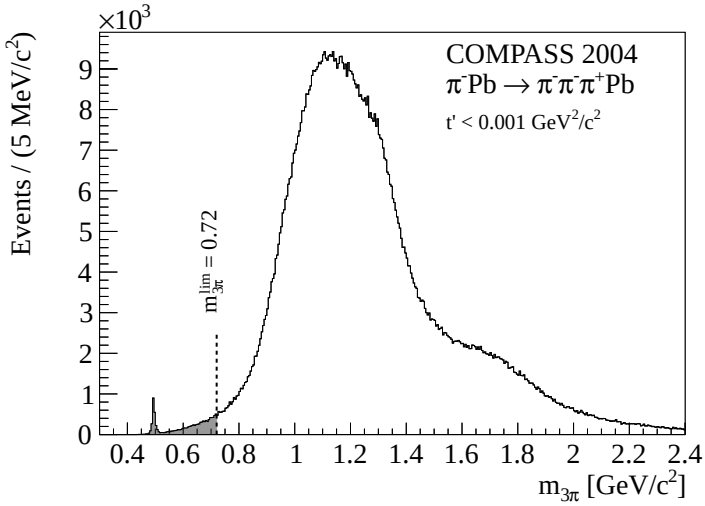

Figure 7: Mass spectrum for the reaction $\pi^-\,\mathrm{Pb} \to \pi^-\pi^-\pi^+\,\mathrm{Pb}$ in the Primakoff region $Q^2 = t' < 0.001\,\mathrm{GeV}^2/c^2$. Events from the decay of the kaons in the incident beam are seen as a peak at $m_{3\pi} = m_{K^-} \approx 0.49\,\mathrm{GeV}^2/c^2$. The region of interest for chiral dynamics up to $m_{3\pi} = 5m_\pi \approx 0.72\,\mathrm{GeV}^2/c^2$ is highlighted in grey.

In order to compare on the absolute level, a flux normalization for the data has to be determined. Here, the kaon component of the hadron beam is used, since some of the kaons decay in the free space around the target with well-known branching into the same three-pion final state as under study here, also with small (rather vanishing) momentum transfer. Dividing by the fraction of kaons to pions in the beam, the effective flux of pions is deduced from the observed kaon decays. Measuring the same final state, it features obviously a similar reconstruction efficiency, that has to be propagated to the full mass spectrum of interest only moderately by the Monte Carlo simulation of the setup.

The result is published in [18]. The absolute cross-section has been determined in five bins of the final-state mass from threshold at $3m_\pi$ up to $5m_\pi$. The data agree with the expectation from tree-level ChPT on the level of the experimental uncertainty of 20%. This confirms, on the one hand, the extension of the ChPT approach for processes involving the coupling of four pions, *i.e.* the leading order, to processes involving the additional coupling to a photon. On the other hand, it demonstrates that the Primakoff technique in the form of Eq. 2.1 can be safely employed. In terms of studying ChPT, the neutral channel $\pi^-\gamma \to \pi^-\pi^0\pi^0$ will be of higher relevance, since for this channel higher-order loop corrections are expected to play a larger role [19].

For determining the ChPT intensity present in the mass range of interest, it has been fitted to the data in its fully (5D) differential form employing the partial-wave analysis techniques as developed and used for extracting contributions from resonances with specific J^{PC} quantum numbers as discussed in the following.

5.2 Radiative coupling of resonances in $\pi^-\gamma \to \pi^-\pi^-\pi^+$

The invariant-mass spectrum obtained for the final state $\pi^-\pi^-\pi^+$ from pions scattering off

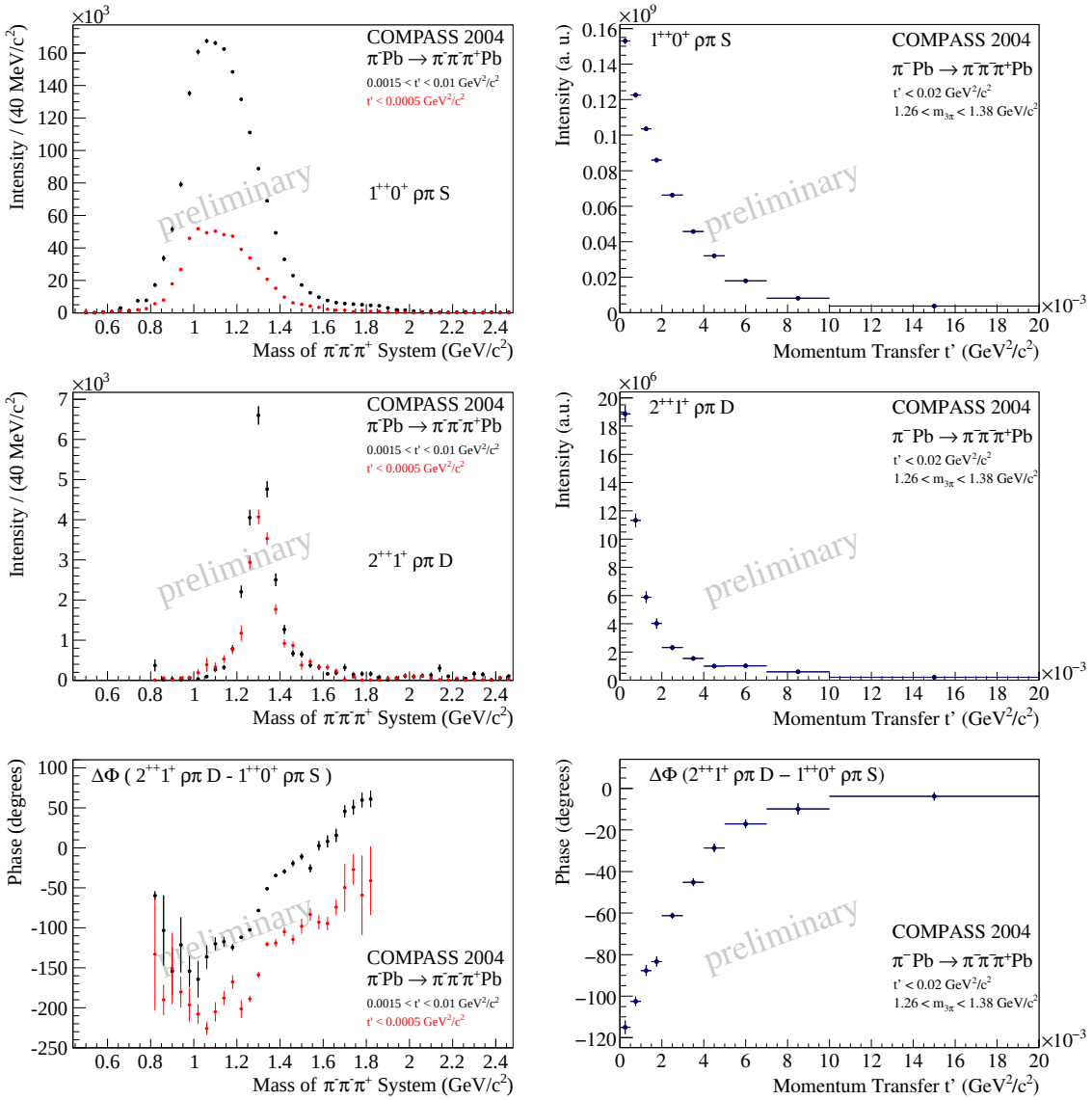

Figure 8: Result of the partial-wave analysis of the data shown in Fig. 7 for the a_1 with $M = 0$ and a_2 with $M = 1$ components. The PWA in mass bins for the low-t' region is shown in the left column for the $1^{++}0^+\rho\pi S$ and the $2^{++}1^+\rho\pi D$ waves, together with their relative phase calculated from the interference term. In the right column, the PWA is performed in t' bins for a broader mass bin covering the main part of the a_2 resonance. The relative phase between the two resonances (lowest-right plot) shifts from about $-110°$ to $0°$, indicating the transition from electromagnetic to strong production of the a_2 resonance. For further details, see text.

lead nuclei at very low momentum transfer $t' < 0.001\,\mathrm{GeV}^2/c^2$ is shown in Fig. 7. It features the salient structures from the well-known resonances $a_1(1260)$, $a_2(1320)$ and $\pi_2(1670)$. For understanding their quantum numbers and the involved production mechanisms, a partial-wave analysis is performed.

It is assumed that the intermediate states, into which the incoming pion is excited through the interaction, are mesonic resonances with well-defined quantum numbers J^{PC}, determined by spin J, parity P and charge-conjugation parity C (in case of charged resonances, the C-parity of the neutral partner in their constituent-quark multiplett). In addition, two more quantum numbers are specified, the spin projection M of J onto the incoming-particle axis (in the *CM* of the resonance), and the reflectivity ε of the transition. The latter expresses, using the parity of the incoming and outgoing system and the involved orbital angular momentum, whether the exchange particle has natural ($J^P = 0^+, 1^-, 2^+, \ldots$ *e.g.* Pomeron, photon) or unnatural ($0^-, 1^+, 2^-, \ldots$ *e.g.* pion) quantum numbers.

Next, it is assumed that the decay of the resonance R into the observed three pions goes through some *isobar* configuration, such that the decay proceeds in fact in two steps of two-body decays. In the first step, the resonance decays into a bachelor pion and a two-pion isobar resonance r, *i.e.* $R \to \pi r$, where r, for the mass range of interest, is typically a $\rho(770)$ or an $f_2(1270)$. In the second step, the isobar decays into two pions, $r \to \pi\pi$. A specific spin configuration in such a resonance decay is thus given by $J^{PC} M^{\varepsilon} r \pi L$, where L determines the orbital angular momentum between r and the bachelor π in the first decay step.

All such excitations to existing resonances that decay into three pions, give rise to an amplitude that contributes to the total transition probability. It is obtained by squaring the total amplitude, to which the single amplitudes sum up.

The key feature of PWA is that due to their quantum numbers, the contributing resonance decays have different angular patterns in the 5-dimensional decay volume. The correlations between the variables is sufficiently high, such that even with a limited knowledge of the three-pion distribution, the contributing amplitudes can be deduced without ambiguity. Additionally, due to the squaring of the amplitude sum, the interference terms emerge with also specific angular signature in the three-pion distribution.

The interference terms are useful in a two-fold way: First, they can serve to identify small-resonance contributions. If an amplitude is small with respect to another, overlapping contribution, then the interference term is possibly much larger and can be identified already at lower statistics. Secondly, at this point it becomes relevant that a resonance is described on the quantum-mechanical level by a complex phase, running from 0 (on the low-energetic side of the resonance) through π (on top of the resonance) and approaching 2π when the exciting energy is much higher than the resonance energy. This phase determines the size and the sign of the interference term, or in turn, from knowing the interference term, the phase motion can be concluded.

The result of the PWA decomposition of the low-t' data taking with a 190 GeV pion beam on lead is shown in Fig. 8 for the a_1 and a_2 resonances. The appearence of the a_2 resonance at small t' is special in two ways: First, in strong production via Pomeron exchange the expected t' dependence is $t' \exp(-bt')$ with $b \approx 400(\mathrm{GeV/c})^{-2}$ [18], in contrast to the observed peak at smallest values. This indicates that the resonance is not produced via the strong interaction, but rather by photon exchange following 2.1, which also approaches 0 as $t' \to 0$, however on the

unobservably small scale of the peak structure in the range of $10^{-6}\,\mathrm{GeV}^2/c^2$. Secondly, the data allow for determining the phase between the two resonances as explained above, and by this the change of production mechanism for the a_2 from electromagnetic to strong production becomes explicit: While the difference between the (real) production of the a_2 via photon exchange and the (imaginary) production of the a_1 via Pomeron exchange leads to the phase difference in the range of -90° for smallest momentum transfers, this difference vanishes at higher momentum transfer, when both production mechanisms turn to strong interaction.

Having ensured that the a_2 is produced via $\pi\gamma$ coupling, the measurement of the absolute cross-section for this process allows the determination of the radiative coupling of the resonance. The required normalization is obtained analogously to the procedure described above, using the Monte Carlo simulation in order to extrapolate the acceptance from the kaon mass to the resonance mass. This analysis is momentarily being finalized. COMPASS has observed with the same method the radiative coupling of the π_2 resonance, and further constraints on radiative couplings of mesonic resonances are in reach.

6. Summary

In summary, several reactions for testing the chiral dynamics, that are accessible with the COMPASS experiment at CERN, have been discussed. The measurement of the pion polarisability reveals a value in agreement with the prediction of ChPT, and in contradiction to previous measurements. In the process $\pi\gamma \to 3\pi$, chiral dynamics at low relative momenta could be observed. At higher energies, it was demonstrated that COMPASS can determine radiative couplings of meson resonances with unprecedented precision.

References

[1] H. Primakoff, Phys. Rev. **81**, 899 (1951).

[2] N. Kaiser and J. M. Friedrich, Eur. Phys. J. **A36**, 181 (2008).

[3] Yu. M. Antipov *et al.*, Phys. Lett. **B121**, 445 (1983).

[4] N. Kaiser and J. M. Friedrich, Eur. Phys. J. **A39**, 71 (2009).

[5] N. Kaiser and J. M. Friedrich, Nucl. Phys. **A812**, 186 (2008).

[6] N. Kaiser, Nucl. Phys. **A837**, 87 (2010).

[7] J. Ahrens *et al.*, Eur. Phys. J. **A23**, 113 (2005).

[8] D. Babusci *et al.*, Phys. Lett. **B277**, 158 (1992).

[9] J. F. Donoghue and B. R. Holstein Phys. Rev. **D48**, 137 (1993).

[10] A. E. Kaloshin and V. V. Serebryakov, Z. Phys. **C64**, 689 (1994).

[11] L. V. Fil'kov and V. L. Kashevarov, Phys. Rev. **C73**, 035210 (2006).

[12] B. Pasquini, D. Drechsel and S. Scherer, PoS of "Chiral Dynamics 09", Bern, 037 (2009).

[13] B. Pasquini, D. Drechsel and S. Scherer, Phys. Rev. **C81**, 029802 (2010).

[14] J. Gasser, M. A. Ivanov and M. E. Sainio, Nucl. Phys. **B745**, 84 (2006).

[15] J. Beringer *et al.* [Particle Data Group], Phys. Rev. **D86**, 010001 (2012).

[16] T. Nagel, PhD thesis, Tech. Univ. München (2012), CERN-THESIS-2012-138, http://cds.cern.ch/record/1484476.

[17] S. Grabmüller, PhD thesis, Tech. Univ. München (2012), CERN-THESIS-2012-170, http://cds.cern.ch/record/1492155

[18] C. Adolph *et al.* [COMPASS Collaboration], Phys. Rev. Lett. **108**,192001 (2012).

[19] N. Kaiser, Nucl. Phys. **A848**, 198 (2010).